1 **Structural insights into the mechanism of the human SGLT2–MAP17 glucose**

2 **transporter**

3

4 Masahiro Hiraizumi[1,4,†,*], Tomoya Akashi[2,4], Kouta Murasaki[1], Hiroyuki Kishida[1],

5 Taichi Kumanomidou[1], Nao Torimoto[1], Osamu Nureki[3,*], and Ikuko Miyaguchi[1,*]

6

7 [1]Discovery Technology Laboratories Sohyaku Innovative Research Division, Mitsubishi

8 Tanabe Pharma Co., LTD., 1000, Kamoshida-cho, Aoba-ku, Yokohama 227-0033, Japan

9 [2]DMPK Research Laboratories Sohyaku Innovative Research Division, Mitsubishi

10 Tanabe Pharma Co., LTD., 1000, Kamoshida-cho, Aoba-ku, Yokohama 227-0033, Japan

11 [3]Department of Biological Sciences, Graduate School of Science, The University of

12 Tokyo, 7-3-1 Hongo, Bunkyo-ku, Tokyo 113-0033, Japan

13 [4]Co-first authors

14 *Corresponding authors

15 Masahiro Hiraizumi: 0000-0002-4340-2937

16 Osamu Nureki: 0000-0003-1813-7008

17 Ikuko Miyaguchi: 0000-0003-0021-7296

18 [†]Current address: Department of Chemistry and Biotechnology, Graduate School of

19 Engineering, The University of Tokyo

Abstract

Selective sodium-glucose cotransporter 2 (SGLT2) plays an important role in glucose reabsorption. SGLT2 inhibitors suppress glucose reabsorption from the kidneys, thus reducing blood glucose levels in type 2 diabetes patients. We and other groups have developed several SGLT2 inhibitors starting from a natural product, phlorizin, but their action mechanisms remain unknown. Here, we elucidated the physiological hSGLT2–MAP17 complex structures bound to five SGLT2 inhibitors using single-particle cryo-electron microscopy. Canagliflozin, dapagliflozin, TA-1887, and sotagliflozin were bound in the outward-facing structure, whereas phlorizin was bound in the inward-open structure. The phlorizin–hSGLT2 interaction biochemically exhibited biphasic binding. Phlorizin weakly binds, via the phloretin motif, from its intracellular side near the Na^+-binding site, while strongly interacts from its extracellular side. Unexpectedly, bound Na^+ stabilizes the outward-open conformation, while its release allows the transporter to adopt inward-open state. Our results first visualized the Na^+-binding and inward-open conformation of hSGLT2–MAP17, clarifying the unprecedented Na^+-dependent sugar transport mechanism with MAP17 acting as a scaffold, and may pave the way for development of next-generation SGLT inhibitors.

Introduction

Type 2 diabetes mellitus is characterized by persistent hyperglycemia caused by inadequate insulin action. Chronic high blood sugar level damages blood vessels, causing serious health problems, such as nephropathy and cardiovascular disease. The primary treatment for diabetes is blood glucose control; drugs such as selective

44   sodium-glucose cotransporter (SGLT1 and 2; also known as SLC5A1 and 2) inhibitors[1]

45   hold great promise for reducing blood glucose levels. Human SGLT1 and SGLT2 are

46   responsible for the reabsorption of plasma glucose in the proximal tubules after

47   filtration through the renal capillaries[2]. SGLT2 is located in the S1 and S2 segments of

48   the proximal tubule and absorbs 90% of plasma glucose; SGLT1, which has higher

49   glucose affinity, is located in the S3 segment of the proximal tubule and absorbs the

50   remaining 10%[3].

51   SGLT2, a transmembrane protein with 14 helices (Fig. 1a) and expressed

52   specifically in the kidneys, has 60% sequence homology to SGLT1, which is expressed

53   in the small intestine as well. SGLT2 inhibitors that suppress glucose reabsorption and

54   promote urinary excretion are considered a promising therapeutic tool to manage blood

55   glucose levels in type 2 diabetes patients. SGLT2 inhibitor development initially

56   focused on the natural product phlorizin (Figs 3b)[4], an O-glucoside that is hydrolyzed

57   by β-glucosidase in the intestine, making oral administration difficult owing to its poor

58   metabolic stability. This was replaced by N- or C-glucosides, with better metabolic

59   stability. C-glucosides, including canagliflozin, dapagliflozin, and empagliflozin, are

60   marketed as approved drugs in USA, Japan and many countries (Figs 1b, 2g, h)[5].

61   SGLT2 inhibitors have ushered in a new phase of diabetes treatment, providing many

62   benefits including, reduced risk of heart failure and kidney protection[6–9]. It was initially

63   thought that rare mutations in the Na^+–glucose cotransporter gene *SLC5A1* can cause

64   lethal glucose–galactose malabsorption and that inhibitors with high specificity for

65   SGLT2 over SGLT1 were necessary to treat diabetes. However, SGLT1 inhibition in the

66   gastrointestinal tract leads to postprandial glucose excursion control and gastrointestinal

67   hormone secretion[10]. Therefore, SGLT1 and SGLT2 dual inhibitors (e.g., sotagliflozin

68   and LX-2761; Fig. 2e) are currently being developed for the treatment of diabetes[9,11].

69   SGLT1 and SGLT2 belong to the LeuT transporter family and are conserved

70   in all bacterial and animal taxa, with six isoforms in humans[12,13]. Structural homology

71   modeling studies have been conducted using SGLT from *Vibrio parahaemolyticus*

72   (vSGLT) and similar protein structures, such as SiaT[14,15], because of the difficulties in

73   protein preparation and structural analysis. A functional model of SGLT2 glucose

74   uptake has been proposed: SGLT2 undergoes a conformational change to an

75   outward-facing conformation by binding to a single Na^+ ion (at Na2 site[16]) before

76   binding to the substrate, depending on Na^+ concentration gradient across the plasma

77   membrane, which then promotes glucose binding. Subsequently, Na^+ and sugars are

78   incorporated into the cell in an inward-open conformation[3,12,13]. In contrast, SGLT1

79   requires two Na^+ ions (at Na2 and Na3 sites) for glucose transport, which probably

80   affects its glucose affinity[16]. The structural understanding of the human SGLT family

81   was advanced by the cryo-electron microscopy (cryo-EM) structures of SGLT1 and

82   SGLT2. The structure of the hSGLT1 apo-form with consensus stabilizing mutations

83   and molecular dynamics calculations, revealed the mechanism of glucose binding and

84   selectivity and water permeability[17]. The activity of hSGLT2, whose gene has long been

85   difficult to clone, is greatly enhanced by the co-expression of MAP17 (PDZK1P1), an

86   essential auxiliary subunit of hSGLT2[18]. Determination of the hSGLT2 structure via

87   MAP17 tethering and the introduction of several mutations revealed that it is bound by

88   empagliflozin in an outward-facing conformation[19]. Furthermore, introduction of

89   MAP17 tethering and several mutations in hSGLT1 revealed that the dual inhibitor

90   LX2761 was bound in the outward conformation of hSGLT1[20]. The role of amino acid

91   residues in the binding of SGLT inhibitors in these two outward conformations was

92　discussed. However, the function of Na^+ remains unknown, because these previous

93　studies did not detect Na^+, which should bind to hSGLT before binding to the substrate.

94　Regarding the binding mode of inhibitors, only C-glucoside inhibitors have been shown

95　to bind in the outward conformation, while the binding mode of O- and N-glucoside

96　type inhibitors, including phlorizin, still needs to be elucidated. Moreover, the

97　conformational changes of SGLT2 between the outward and inward conformations as

98　well as the role of MAP17 as a scaffold have yet been unclarified.

99　　　　Here, we performed cryo-EM single-particle analyses to determine the

100　structure of the genuine hSGLT2–MAP17 complexes with five inhibitors (canagliflozin,

101　dapagliflozin, TA-1887, sotagliflozin, and phlorizin). This characterization of

102　Na^+-binding outward-facing structures and inward-open structures with MAP17 as a

103　scaffold, together with transport and binding assays, significantly clarifies the molecular

104　features of hSGLT2–MAP17, SGLT2 inhibition, and sugar transport, which helps

105　achievement of glycemic control in patients.

106

107　**Results and discussion**

108　***Structural determination of the hSGLT2–MAP17 heterodimer***

109　We performed cryo-EM analysis of hSGLT2 to elucidate its inhibitory mechanism. To

110　obtain a stable and homogeneous sample, we first examined, by fluorescence-detection

111　size-exclusion chromatography (FSEC)[21], the expression of hSGLT2 whose N or C

112　terminus was fused with enhanced green fluorescent protein (EGFP). However, we were

113　unable to detect hSGLT2 expression (Fig. 1c); given that its N-terminus is exposed to

114　the extracellular side, we hypothesized that N-terminal fusion of a signal sequence and

115　super folder GFP (sfGFP) would improve the protein expression[22]. Fusing the human

5

116   trypsinogen 1-derived signal peptide and sfGFP to the hSGLT2 N-terminus revealed a

117   peak, indicating that hSGLT2 can be solubilized by detergents (Fig. 1c). Co-expression

118   of MAP17 and hSGLT2 caused a high molecular-weight shift in FSEC, suggesting

119   heterodimer-complex formation. LC-MS/MS confirmed that signal peptides and sfGFP

120   fused with hSGLT2–MAP17-expressing cells could take up

121   α-methyl-D-glucopyranoside (α-MG; Fig. 1b); this uptake was sensitive to canagliflozin

122   (Fig. 1d). We used LC-MS/MS to determine whether the prepared membrane fractions

123   maintained their inhibitor-binding activity, verifying the binding of multiple inhibitors

124   to hSGLT2 (Fig. 1e; Supplementary Fig. 1c). Membrane fraction of

125   hSGLT2–MAP17-expressing cells was solubilized with N-dodecyl β-d-maltoside

126   (DDM) micelles in the presence of SGLT2 inhibitors, purified using GFP

127   nanobody-affinity chromatography, followed by cleavage of sfGFP using protease, and

128   subjected to gel-filtration column chromatography (Supplementary Fig. 1a, b).

129   Purified hSGLT2–MAP17 complexes were subjected to cryo-EM

130   single-particle analyses with five inhibitors (canagliflozin, dapagliflozin, TA-1887,

131   sotagliflozin, and phlorizin; Supplementary Figs 3–6, 8). The acquired movies were

132   motion-corrected and processed in RELION[23,24] providing cryo-EM maps at overall

133   resolutions of 2.6–3.3 Å, according to the gold-standard Fourier shell correlation (FSC)

134   = 0.143 criterion (Supplementary Data Table 1). All of the potential maps contained

135   disordered regions but were sufficient for building structural models of proteins and

136   inhibitors (Supplementary Figs 7, 9). The overall structure exhibits a LeuT fold

137   comprising 14 membrane-spanning helices (TM0–TM13). Helices TM1–5 and TM6–10

138   formed an inverted repeating structure (Fig. 1a). N-glycan, attached to N250 of hSGLT2,

139   was identified (Supplementary Figs 7, 9). Canagliflozin, dapagliflozin, sotagliflozin,

140   and TA-1887 were found to bind to the outward-facing conformation, whereas phlorizin

141   was found to bind to the inward-open conformation. Because of their high flexibility,

142   the N-terminal loop of hSGLT2 (15–20 amino acids), the IL6 loop between TM12 and

143   TM13, and the extracellular or intracellular region of MAP17, were not visible in either

144   structure. The inward-open structure does not exhibit density for IL0 between TM0 and

145   TM1. In MAP17, a single transmembrane helix interacts with TM13 of hSGLT2,

146   consistent with the published interaction between MAP17 and hSGLT2[19]. The

147   extracellular half interacts closely with hydrophobic residues and lipids, while the

148   intracellular half does not interact with hSGLT2 (Fig. 1f; Supplementary Fig. 10).

149

150   ***The inhibitor-bound hSGLT2 structure and the roles of the Na2 site***

151   The C-glucoside inhibitors (canagliflozin, dapagliflozin, and sotagliflozin), and the

152   N-glucoside TA-1887, are bound to the central hydrophobic cavity of the topologically

153   inverted repeats (IRs) (TM1, TM2, TM3, TM6, and TM10; Figs 1a, 2a) of hSGLT2 in

154   outward-facing conformation. This cavity was negatively charged, favoring the binding

155   of positively charged ions such as Na^+. The binding mode was the same as that in the

156   recently reported SGLT2-empagliflozin structure[19]; for the main chain, with

157   root-mean-square deviation (RMSD) ranging from 0.66 to 0.85 Å.

158   SGLT2 couples the transport of one Na^+ ion and one glucose molecule. The

159   Na^+-binding Na2 site, which is conserved in many LeuT-fold transporters, was located

160   near the middle bend of TM1 (Fig. 2b). In SGLT2, the Na2 site is thought to be formed

161   by the backbone carbonyls of A73, I76, and A389 and the side chain oxygens of S392

162   and S393 (Fig. 2b), based on the vSGLT[15] and SiaT[25] alignment (Supplementary Fig. 2).

163   The density corresponding to Na^+ at the Na2 site was confirmed in all four

164 outward-facing structures studied here (Supplementary Fig. 11). As predicted from the

165 alignment, Na^+ interacts with A73 and I76 of TM1 and with A389, S392, and S393 of

166 TM8, resulting in a trigonal bipyramidal form (Fig. 2b). Thus, TM1 and TM8 are

167 connected by Na^+ and form part of the substrate-binding site. In the outward-facing

168 structure, this connection not only brought TM1 and TM8 closer together but also

169 allowed the entire outer region of the glucose-binding site, such as TM5, to move

170 outward, causing the inward-open to outward-facing conformational change (Fig. 2c).

171 The binding affinity of canagliflozin to hSGLT2 was lower in the Na^+ absent conditions

172 (Fig. 2d, Supplementary Data Table 2). Therefore, Na^+ binds to hSGLT2 before the

173 substrate or inhibitors binding, allosterically stabilizing the outward-facing structure.

174 Our current findings first clarified the role of sodium ions in the transport state

175 exchange. This is consistent with the fact that, in SGLT1, substitutions of S392 and

176 S393 at the Na2 site significantly reduced glucose uptake[26].

177

Implication of the role of Na3 site of SGLT1

179 SGLT1 requires two Na^+ ions for sugar transport and has an Na3 site in addition to the

180 Na2 site[3]. In SGLT2, the region corresponding to SGLT1 Na3 site, located on the

181 cytoplasmic side and away from the glucose-binding pocket, is occluded by the side

182 chain carboxyl group of D201 in TM5 and the backbone carbonyls of S392, S393, A395,

183 and S396 in TM8 (Fig. 3c and Sup. Fig. 2 and 11b). In SGLT1, the residue

184 corresponding to A395 in hSGLT2 is replaced by Thr, which probably contributes to

185 Na^+ binding[17]. This is consistent with the fact that no density corresponding to Na^+ was

186 observed at the Na3 site in the present hSGLT2 structures (Supplementary Fig. 11b).

8

187   It has been proposed that, as at the Na2 site, Na$^+$ at the Na3 site binds before

188   substrate binding and is taken up by the cell before the substrate[14]. In the present

189   outward-facing structure of hSGLT2, the region corresponding to SGLT1 Na3 site is

190   located very close to Na2 site so as to partially share the same amino acid residues,

191   suggesting that the Na3 site, in addition to Na2 site, of SGLT1 also stabilizes the

192   outward-open, substrate-binding structure by connecting TM1 to TM5, as Na2 connects

193   TM1 and TM8 in SGLT2. Taken together, this may contribute to the higher affinity of

194   SGLT1 for its substrate[16] but its slower turnover relative to SGLT2[27].

195

196   ***The hSGLT2 outward-facing conformation in complex with inhibitors***

197   SGLT2 inhibitors were composed of glucose and aglycone moieties (Fig. 1b). The

198   aglycone moiety comprises two aromatic rings that bend at the methylene bridge and

199   extend toward the extracellular space (Fig. 2a, b). The glucose moiety of all gliflozin

200   inhibitors stacks with the aromatic side chain of the inner gate, Y290. The hydroxyl

201   groups of the glucose moiety form hydrogen bonds in the side chains of N75, H80, E99,

202   S287, W291, K321, and Q457, and in the main chain carbonyl group of F98 (Fig. 2b);

203   these residues were conserved in SGLT1 (Supplementary Fig. 2). A water molecule-like

204   density was observed near S460 in the structures of canagliflozin, dapagliflozin, and

205   TA-1887 (Fig. 2b and Supplementary Fig. 7). It has been reported that the

206   corresponding T460 mutant of SGLT1 has reduced sugar transport activity[28]. Therefore,

207   these S460-bound water molecules may also participate in D-glucose transport in

208   hSGLT2.

209   The IC50 values of the five compounds for hSGLT2 were 1–6 nM, with little

210   difference, while sotagliflozin, an SGLT1/2 dual inhibitor, had >10-fold stronger

211   activity toward SGLT1 (IC50 of 40 nM) than the other inhibitors[6]. Sotagliflozin has a

212   methylsulfanyl group at C5 of glucose, whereas dapagliflozin has a hydroxymethyl

213   group which has a hydrogen bonding interaction with Gln457 and a water

214   molecule-mediated interaction with S460 (Fig. 2e, g, Supplementary Fig. 7). In SGLT1,

215   S460 of hSGLT2 near C5 was replaced by Thr, V286 by Leu, and L283 by Met, causing

216   the inhibitor-subtype selectivity[19].

217   In all of the gliflozin inhibitors, the central aromatic ring is exposed to the

218   hydrophobic cavity formed by TM1, TM3, and TM10 (Figs. 2e-h): in TA-1887, this is a

219   benzylindole ring, which extends into the hydrophobic cavity (Fig. 2f). The

220   hydrophobic substituents at the para position affect hSGLT2 inhibitory activity[29,30], and

221   are all located at approximately the same position (Fig. 2a, b, and e–h). V157, located in

222   TM3 in hSGLT2, is replaced by A160, smaller than Val, in hSGLT1. This site is

223   potentially selective for hSGLT2, because the hydrophobic pocket sizes should be

224   different. Molecular dynamics simulation frames in the hSGLT1 with mizagliflozin

225   showed that A160 is important for the selectivity, which is consistent with the present

226   results[31].

227   Distal aromatic rings form a long hydrophobic aglycon tail that extends into

228   the extracellular vestibule. In all gliflozins, each tail formed a T-shaped π-π stacking

229   with F98 of TM2 and was surrounded by hydrophobic amino acids such as Leu84 of

230   TM1, V95 of TM2, and F453 of TM10 (Fig. 2b, e–h). Canagliflozin extends with

231   fluorophenyl via a thiophene ring, forming a hydrophobic interaction with the

232   extracellular vestibule (Fig. 2b). Structure-activity relationship studies during the

233   development of canagliflozin showed that its inhibitory activity increases with furan

234   replaced by thiophene in the center[25], suggesting that this moiety should be hydrophobic.

235　Thus, F98 and F453 are suggested to play important roles in the inhibitory action. It has

236　been reported that SGLT1 has I98 at the position corresponding to V95 in hSGLT2 TM2,

237　and that V95I reduced the inhibitory activity of empagliflozin in hSGLT2[19]. The distal

238　aromatic rings also contribute to the selectivity between hSGLT1 and hSGLT2[8].

239

240　***High concentration phlorizin fixes hSGLT2 in the inward-open state.***

241　Unexpectedly, phlorizin was found to bind to TM1, TM5, and TM8 in an inward-open

242　structure (Fig. 3a), in contrast to the above gliflozins. This binding site is located near

243　the Na2 site, where sodium ions bind to the outward-facing structure (Fig. 2b). The

244　corresponding site is occluded in the inward-facing state of vSGLT and SGLT1

245　(Supplementary Fig. 12)[15,17], and a PEG molecule was observed in the same location in

246　the inward-open structure of vSGLT (Supplementary Fig. 12)[14]. The glucose moiety of

247　phlorizin is bound to the bending site of the intracellular side of TM1, whereas the

248　aglycon moiety, connected to the glucose moiety via an ether bond, is surrounded by the

249　side chain of A69, S70, A73 and S74 of TM1, D201 of TM5, and R300 of TM6,

250　extending toward the lipid membrane (Fig. 3c). The ether bond is unique to phlorizin,

251　whereas the central aromatic ring of gliflozins connects directly to the glucose moiety,

252　causing rigidity that prevents binding to the inward-opening structure.

253　　　　The binding of phlorizin to the hSGLT2 expressing membrane fraction at up

254　to 5000 nM did not saturate and exhibit biphasic kinetics, indicating that phlorizin has

255　two binding sites on hSGLT2 (high- and low-affinity sites; Fig. 3d–f). Similarly, the

256　binding of [³H]phlorizin exhibits biphasic binding in rat renal plasma membrane[33]. In

257　whole-cell clamp experiments, hSGLT2 inhibitors, including phlorizin, achieve

258　inhibition by acting on the extracellular side[34,35]; but phlorizin is the only one that has

259　been reported to act weakly from the intracellular side at high concentrations[34].

260　Inhibition from the inside is more potent when there is no intracellular or extracellular

261　Na^+ concentration gradient[34]. Here, we added high concentration (500 µM) of phlorizin

262　to the hSGLT2–MAP17 solution during the purification process, with no Na^+ gradient;

263　cryo-EM captured the binding state of phlorizin accessing from the intracellular side.

264　We examined the binding activity and transport function of hSGLT2 alanine mutants of

265　residues S74 or D201 involved in phlorizin binding in the inward-open structure, and of

266　F98 or F453 involved in the inhibitor interactions in the outward-facing structure of

267　hSGLT2. Based on FSEC, all mutants (including the WT) preserved their conformation

268　(Supplementary Fig. 1d).

269　　　　Unexpectedly, the F98A and F453A single mutants did not bind to phlorizin

270　(Fig. 3e); F98 and F453 not only participate in the inhibitor binding in the

271　outward-facing conformation, but also form π-π stacking interactions with each other in

272　the inward-open conformation, which is probably important for maintaining the

273　inward-open state (Fig. 3c). The low-affinity binding phase of phlorizin was lost in both

274　the S74A and D201A mutants, with phlorizin binding only to the high-affinity site of the

275　WT (Fig. 3e, f, Supplementary Data Table 3). Phloretin, the aglycon tail of phlorizin,

276　binds to the WT as well as phlorizin but not to the S74A and D201A mutants (Fig. 3g).

277　Therefore, S74A and D201A have lost the ability to bind phlorizin on the cytoplasmic

278　side but can still bind it on the extracellular site. Since the S74A, F98A, and F453A

279　mutants maintained α-MG uptake (Fig. 3h), we performed experiments to inhibit sugar

280　uptake using phlorizin. Inhibition of α-MG uptake by phlorizin was greatly impaired in

281　the F98A and F453A mutants, which lacked phlorizin-binding ability, but was

282　maintained in the S74A mutant, in which the outer binding site was functional (Fig. 3i,

283   Supplementary Data Table 4). No clear uptake of α-MG was observed in the D201A

284   mutant (Fig. 3h). D201 corresponds to D204 in hSGLT1, which is involved in the Na3

285   site formation and is important for sugar uptake activity and cell trafficking; it is

286   expected to play a similar role in hSGLT2[36]. These results support the previous

287   suggestions that phlorizin strongly and weakly inhibits hSGLT2 from the extracellular

288   and intracellular sides, respectively.

289

290   ***Structural rearrangement from the outward to inward conformations***

291   Given that hSGLT2 exhibits outward and inward conformations, we will consider its

292   structural changes during sugar transport. TM1-10 is conserved in the LeuT family.

293   hSGLT2 contains a bundle domain comprising TM1, -2, -6, and -7, a hash domain

294   comprising TM3, -4, -8, and -9, and two gating helices, TM5 and -10. In addition, the

295   core of hSGLT2 was surrounded by TM0, TM11–13, and MAP17 (Fig. 4).

296   The bundle domain of LeuT-fold transporters such as Mhp1 and vSGLT1 is

297   reportedly fixed, while the hash domain and gating helices rotate to transport substrates

298   via an alternating-access mechanism[12]. When the bundle domains are superimposed

299   between the inward and outward structures, TM13 and MAP17 are also well

300   superimposed, while the other parts of the transporter change their location and

301   conformation (Fig. 4a, Supplementary Movie 1). MAP17 is expected to affect the active

302   conformation of hSGLT2, because its co-expression enhances hSGLT2 activity, without

303   altering hSGLT2 expression on the plasma membrane[18]. However, the present structure

304   suggests that MAP17 stabilizes the bundle domain together with TM13, as a scaffolding

305   protein in the plasma membrane (Fig. 4a).

306   The substrate-binding site and external vestibule are formed by TM1, -2, -6,

307   and -10 in the outward-facing conformation (Fig. 4b, c). Y290 in TM6, N75 in TM1,

308   and K154 in TM3 form π-cation interactions, where the corresponding interaction of

309   vSGLT1 is thought to act as an inner gate for substrates. SGLT1/2 has a characteristic

310   Pro-Pro motif (465, 466) in the middle of TM10, causing a bend in the α-helix (Fig. 4c,

311   e). This causes F453 of TM10 to form a T-shaped π–π interaction with F98 of TM2 in

312   the inward-open conformation; the external vestibule is covered by this interaction, and

313   by L84 of TM1 (Fig. 4e). These residues are thought to act as external gates for

314   transporters. The binding of the distal aromatic ring to the outward-facing conformation

315   moves the F453 side chain of TM10 to the opposite side, and instead the distal aromatic

316   ring forms a tight interaction with F98 of TM2, thus inhibiting the inward transition

317   (Supplementary Movie 1). This is consistent with the reduced binding activity of

318   SGLT2 inhibitors in the F98A and F453A mutants (Supplementary Fig. 1e).

319   The inward-open structure, which has no Na^+ bound, is thought to mimic the structure

320   once Na^+ and the substrate are transported into the cytoplasmic side[14]. With the

321   movement of the hash domain and gating helices, the interaction between K154 of TM3

322   and Y290 of TM6 is broken (Fig. 4c, e), and TM8 moves so that it fills the space

323   partially occupied by TM3. Furthermore, TM8 and the intracellular part of its

324   connecting TM9 outwardly shift significantly. The small-loop structure of IL0 stabilizes

325   the outward-facing structure from the intracellular side, together with a cation-π

326   interaction between R427 and Y55, which becomes lost and disordered in the

327   inward-open conformation. In SGLT1 and vSGLT, the small helical structure IL0 in the

328   inward-open conformation is also disordered [14,17], and is therefore thought to be

329   conserved among these proteins.

14

330   Because phlorizin was bound to the low-affinity binding site in the

331   inward-open conformation under these experimental conditions, we suggest that, in the

332   absence of an Na^+ concentration gradient, hSGLT2 is stabilized in the inward-open

333   conformation, and that the Na^+ concentration gradient may promote sodium binding to

334   the Na2 site. Although this study does not fully elucidate the dynamics of Na^+

335   binding/release and sugar uptake, it reveals that sugar uptake depends on the change

336   from the outward-facing to the inward-open conformation, and that groove formation by

337   the inward-open structure without Na^+ binding is the driving force of sugar uptake.

338   Based on molecular dynamics studies of vSGLT, sugar uptake occurs after Na^+ is

339   released[14], which is consistent with our findings. After the uptake of sugar and sodium

340   is completed in the inward-open state of the protein, the sodium concentration gradient

341   drives the change toward the outward-open conformation, allowing the next sodium ion

342   to be accepted, thus rotating the glucose transport cycle. Our structural findings

343   therefore provide support for the proposed Na^+-glucose co-transport mechanism.

344   In summary, we have elucidated the structures of five

345   hSGLT2–MAP17-inhibitor complexes using cryo-EM, in addition to the

346   sodium-binding outward-facing and inward-open structures of hSGLT2 and a two-phase

347   mode of inhibition. This allowed us to identify the unprecedented role of Na^+ ions in

348   regulating transport state dynamics (Fig. 5). Most sodium-bound symporters of the

349   LeuT family share their Na2 site and domain structures and may employ a common

350   transport mechanism. We believe that our findings will help us to better understand the

351   molecular mechanism of action of this transporter family and to develop new drugs that

352   target disease-related transporters.

15

353

Methods

Reagent and Chemicals

356 Canagliflozin and TA-1887 were synthesized by Mitsubishi Tanabe Pharma Corporation

357 (Yokohama, Japan)[32,37]. Dapagliflozin and sotagliflozin were purchased from Cayman

358 Chemical Company (Ann Arbor, MI). Phlorizin, phloretin, and α-MG were purchased

359 from Sigma-Aldrich (St. Louis, MO).

360

Expression and purification of the hSGLT2-MAP17 heterodimer

362 hSGLT2 (UniProt: P31639-1) cDNA and human MAP17 (UniProt: Q13113-1) cDNA

363 were synthesized and codon-optimized for expression in human cell lines. Both cDNAs

364 were cloned into pcDNA3.4 vector. The hSGLT2 sequence was fused with an

365 N-terminal signal sequence from human trypsinogen 1, a His10 tag, and super-folder

366 green fluorescent protein (sfGFP), followed by a human rhinovirus 3C protease

367 (HRV3C protease) recognition site. Point mutations were introduced into this construct

368 using site-directed mutagenesis.

369 Mammalian Expi293 cells (Thermo Fisher Scientific, Waltham, MA) were grown and

370 maintained in Expi293 Expression Medium at 37 °C and 8% CO_2 under humidified

371 conditions. Cells were transiently transfected at a density of 2.0×10^6 cells mL^{-1} with

372 the plasmids and FectoPRO (Polyplus, Illkirch-Graffenstaden, France). Approximately

373 320 μg of the hSGLT2 plasmid and 160 μg of the MAP17 plasmid were premixed with

374 720 μL of FectoPRO reagent in 60 mL of Opti-MEM (Gibco) for 10–20 min before

375 transfection. For transfection, 60 ml of the mixture was added to 0.6 L the cell culture

376 and incubated at 37 °C in the presence of 8% CO_2 for 72 h before collection. The cells

16

377   were collected by centrifugation (800 ×g, 10 min, 4 °C) and stored at −80 °C before

378   use. The detergent-solubilized proteins were analyzed by fluorescence-detection

379   size-exclusion chromatography (FSEC) using an ACQUITY UPLC BEH450 SEC 2.5

380   µm column (Waters, Milford, MA).

381   To prepare the complex sample with phlorizin, the cells were solubilized for 1 h at

382   4 °C in buffer (50 mM HEPES-NaOH [pH 7.5], 300 mM NaCl, 2% (w/v)

383   N-dodecyl β-d-maltoside (DDM, Calbiochem, San Diego, CA), protease inhibitor

384   cocktail, and 1 mM phlorizin). After ultracentrifugation (138,000 ×g, 60 min, 4 °C),

385   the supernatant was incubated with Affi-Gel 10 (Bio-Rad, Hercules, CA) coupled with a

386   GFP-binding nanobody[38] and incubated for 2 h at 4 °C. The resin was washed five

387   times with three column volumes of wash buffer (50 mM HEPES-NaOH (pH 7.5),

388   300 mM NaCl, 0.05% DDM (GLYCON Biochemicals, Luckenwalde, Germany), and

389   1 mM phlorizin), and gently suspended overnight with HRV3C protease to cleave the

390   His10-sfGFP tag. After HRV3C protease digestion, the flow-through was pooled,

391   concentrated, and purified by size-exclusion chromatography on a Superose 6 Increase

392   10/300 GL column (GE Healthcare, Chicago, IL), and equilibrated with SEC buffer

393   (20 mM HEPES-NaOH [pH 7.5], 150 mM NaCl, 0.03% DDM [GLYCON], and 0.5

394   mM phlorizin). For the complex samples with canagliflozin, TA-1887, dapagliflozin,

395   and sotagliflozin, the same procedure was performed, but at inhibitor concentrations of

396   30 µM each. The peak fractions were pooled and concentrated to 6–10 mg ml^{-1}.

397

398   ***Methyl α-D-glucopyranoside (α-MG) uptake in hSGLT2-transfected HEK293 cells***

399   HEK293 cells (ECACC 85120602) were maintained in Dulbecco's modified Eagle's

400   medium (Gibco) supplemented with 10% fetal bovine serum (FBS; Thermo Scientific),

401   2 mM l-glutamate, 100 U/mL benzylpenicillin, and 100 µg/mL streptomycin, at 37 °C

402   in a humidified atmosphere of 5% CO_2 in air. HEK293 cells were transiently transfected

403   with 0.25 µg pcDNA3.4 vector containing a MAP17-coding region and 0.50 µg

404   pcDNA3.4 vector containing an hSGLT2-coding region, using Lipofectamine 2000

405   (Life Technologies, Carlsbad, CA), and cultured for 48 h. The medium was removed,

406   and the cells were washed twice, then preincubated with extracellular fluid buffer

407   without glucose (122 mM NaCl, 25 mM $NaHCO_3$, 3 mM KCl, 1.4 mM $CaCl_2$, 2 mM

408    $MgSO_4$, 0.4 mM K_2HPO_4, 10 mM HEPES; pH 7.4) at 37 °C for 20 min. After

409   preincubation, uptake was initiated by replacing the preincubation buffer with

410   extracellular fluid buffer containing 500 µM α-MG in the absence or presence of

411   inhibitors. Uptake was completed by removing the uptake buffer and washing with

412   ice-cold buffer three times, followed by solubilization in 1 N NaOH at room

413   temperature. The uptake of α-MG gradually increased over 60 min (Supplementary Fig.

414   1E) and the incubation time in the inhibition assay was 30 min.

415   Cell lysates were deproteinized by adding acetonitrile containing candesartan as the

416   internal standard. The concentration of α-MG was quantified via LC-MS/MS, using the

417   internal standard method.

418   Specific peaks of α-MG were observed in the lysates of mock cells and

419   hSGLT2-expressing cells incubated with α-MG, but no specific peaks were observed in

420   the lysates of mock cells without the addition of α-MG (Supplementary Fig. 1F).

421   Cellular protein content was determined using a bicinchoninic acid (BCA) protein assay

422   kit (Thermo Fisher Scientific). The uptake of α-MG was expressed as the ratio of

423   pmol/mg protein in the cells to pmol/µL in the medium (cell-to-medium ratio; µL/mg

424   protein).

425 In the inhibition study, the cell-to-medium ratio of cells transfected with the empty

426 vector was used as the background. The specific α-MG uptake was calculated by

427 subtracting the background from the total cell-to-medium ratio and normalized to the

428 uptake achieved without the inhibitor. The three replicates were obtained from the same

429 samples. IC50 was calculated via nonlinear regression using GraphPad Prism 8.4.3.

430

431 ***SGLT2 inhibitor-binding assay by affinity selection-mass spectrometry***

432 To examine the inhibition of binding to the crude membrane, mammalian Expi293 cells

433 were co-transfected with hMAP17 and wild-type hSGLT2 or its mutants, as described

434 above. The cells were collected and disrupted by sonication in a hypotonic buffer

435 (50 mM HEPES-NaOH [pH 7.5], 10 mM KCl, and protease inhibitor cocktail) or

436 Na^+-free hypotonic buffer (50 mM Tris-HCl [pH 7.5], 10 mM KCl, and protease

437 inhibitor cocktail). Cell debris were removed by centrifugation (2,000 $\times g$, 5 min,

438 4 °C). The membrane fraction was collected by ultracentrifugation (112,000 $\times g$, 30

439 min, 4 °C) and stored at −80 °C before use. The crude membrane (250 µg per sample)

440 was incubated with SGLT2 inhibitor in an assay buffer (100 mM NaCl, 10 mM

441 HEPES/Tris, pH 7.4) or Na^+-free assay buffer (100 mM choline chloride, 10 mM

442 HEPES/Tris, pH 7.4) at room temperature for 2 h. Reactions were terminated by

443 filtration through a GF/C filter plate (Corning Inc., Corning, NY) presoaked in assay

444 buffer containing 0.1% BSA. The sample in the filter plate was washed three times with

445 the assay buffer and eluted with acetonitrile : water (80:20, v/v). The extract solution

446 from the filter plate was diluted with water containing candesartan as an internal

447 standard, and the concentration of SGLT2 inhibitors was quantified using LC-MS/MS.

448 Non-specific binding was determined by the membrane fraction of the

449 non-transfected-Expi293 cells, and specific binding was calculated by subtracting the

450 non-specific binding from the binding of hSGLT2-expressing cells. Specific binding

451 was normalized to hSGLT2 protein expression levels, measured by FSEC. The

452 equilibrium dissociation constant (Kd) and maximum number of binding sites (B_{max})

453 were calculated via nonlinear regression in GraphPad Prism 8.4.3. The specific binding

454 of the hSGLT2 mutants was normalized to that of wild-type hSGLT2.

455

456 ***Quantification of SGLT2 substrate and inhibitors via LC-MS/MS***

457 The concentration of the extract solution from the filter plate and cell lysate was

458 quantified using tandem mass spectrometry (QTRAP6500 System (SCIEX,

459 Framingham, MA) coupled with an ACQUITY UPLC system (Waters) using the

460 internal standard method. Mobile phases A and B used 10 mM of ammonium

461 bicarbonate and acetonitrile, respectively. Chromatographic separation was performed

462 on an ACQUITY UPLC BEH C18 column (2.1 mm × 100 mm, 1.7 μm; Waters) at

463 50 °C, with the following gradient of mobile phase B: 1% (at 0.00 to 0.50 min), 1% to

464 95% (0.50 to 2.00 min), 95% (2.00 to 2.50 min), and 1% (2.51 to 3.0 min); the flow rate

465 was 0.4 mL/min. Mass spectrometric detection was performed by multiple reaction

466 monitoring in the electrospray-ionization negative-ion mode, using m/z 443.1 / 364.9

467 for canagliflozin; 425.9 / 264.1 for TA-1887; 407.0 / 328.8 for dapagliflozin; 423.0 /

468 387.0 for sotagliflozin; 435.0 / 273.0 for phlorizin; 273.0 / 148.9 for phloretin; and

469 192.9 / 100.9 for α-MG.

470

471 *Electron microscopy sample preparation*

472 The purified protein solution of hSGLT2–MAP17 was mixed with the inhibitor

473 solutions except for phlorizin, with final concentrations of 0.5 mM dapagliflozin,

474 TA-1887, sotagliflozin, or canagliflozin. After incubation for 1 h on ice, the grids were

475 glow-discharged in low-pressure air with a 10 mA current in a PIB-10 (Vacuum

476 Device, Mito, Japan). The protein solutions containing 0.5 mM of the inhibitors were

477 applied to a freshly glow-discharged Quantifoil Holey Carbon Grid (R1.2/1.3, Cu/Rh,

478 300 mesh)(SPT Labtech, Melbourne Hertfordshire, UK) using a Vitrobot Mark IV

479 (Thermo Fisher Scientific) at 4 °C, with a blotting time of 4–6 s under 99% humidity

480 conditions; the grids were then plunge-frozen in liquid ethane.

481

482 *Electron microscopy data collection and processing*

483 The grids containing phlorizin, TA-1887, dapagliflozin, and sotagliflozin were

484 transferred to a Titan Krios G3i (Thermo Fisher Scientific) running at 300 kV and

485 equipped with a Gatan Quantum-LS Energy Filter (GIF) and a Gatan K3 Summit direct

486 electron detector in the correlated double sampling mode. Imaging was performed at a

487 nominal magnification of 105,000×, corresponding to a calibrated pixel size of 0.83

488 Å/px (The University of Tokyo, Japan). Each movie was dose fractionated to 64 frames

489 at a dose rate of 6.2–9.0 e⁻/px/s at the detector, resulting in a total accumulated exposure

490 of 64 e⁻/Å² of the specimen. The data were automatically acquired using the image-shift

491 method in SerialEM software[39], with a defocus range of −0.8 to −1.6 μm.

492 The grid with canagliflozin was transferred to a Titan Krios G4 device (Thermo Fisher

493 Scientific) running at 300 kV and equipped with a Gatan Quantum-LS Energy Filter

494 (GIF) and a Gatan K3 Summit direct electron detector in correlated double sampling

495   mode. Imaging was performed at a nominal magnification of 215,000×, corresponding

496   to a calibrated pixel size of 0.4 Å/px (The University of Tokyo, Japan). Each movie was

497   recorded for 1.4 seconds and subdivided into 64 frames. Electron flux was set to 7.5

498   e^-/px/s at the detector, resulting in an accumulated exposure of 64 e^-/$Å^2$ of the specimen.

499   The data were automatically acquired via the image-shift method using EPU software

500   (Thermo Fisher Scientific), with a defocus range of −0.6 to −1.6 µm. The total number

501   of images is described in Supplementary Data Table 1.

502   For all datasets, the dose-fractionated movies were subjected to beam-induced motion

503   correction using RELION[23], and the contrast transfer function (CTF) parameters were

504   estimated using CTFFIND4[40].

505   For the canagliflozin-bound state dataset, 2,364,108 particles were initially selected

506   from 19,943 micrographs, using the topaz-picking function in RELION-4.0[24]. Particles

507   were extracted by downsampling to a pixel size of 3.2 Å/px. These particles were

508   subjected to several rounds of 2D and 3D classification. The best class contained

509   221,701 particles, which were then re-extracted with a pixel size of 1.60 Å/px and

510   subjected to 3D refinement. The second 3D classification resulted in three map classes.

511   The best class from the 3D classification contained 179,761 particles, which were

512   subjected to 3D refinement. The particles were subsequently subjected to micelle

513   subtraction and non-aligned 3D classification using a mask (without micelles), resulting

514   in three map classes. The best class, containing 65,919 particles, was subjected to 3D

515   refinement, reversion to the original particles, and 3D refinement. The particle set was

516   resized to 1.00 Å/px, and subjected to Bayesian polishing, 3D refinement, and

517   per-particle CTF refinement before the final 3D refinement and post-processing,

518   yielding a map with a global resolution of 3.1 Å, according to the FSC = 0.143 criterion.

519   Finally, local resolution was estimated using RELION-4. The processing strategy is

520   illustrated in Supplementary Fig. 3.

521

522   For the dapagliflozin-bound-state dataset, 3,692,950 particles were initially selected

523   from 4,841 micrographs, using the topaz-picking function in RELION-4.0. Particles

524   were extracted by downsampling to a pixel size of 3.32 Å/px. These particles were

525   subjected to several rounds of 2D and 3D classification. The best class contained

526   569,516 particles, which were then re-extracted at a pixel size of 1.30 Å/px and

527   subjected to 3D refinement. Non-aligned 3D classification using a soft mask covering

528   the proteins and micelles resulted in four map classes. The best class from the 3D

529   classification contained 197,695 particles, which were subjected to 3D refinement,

530   per-particle CTF refinement, and 3D refinement. The resulting 3D model and particle

531   set were resized to 1.11 Å/px and subjected to Bayesian polishing, 3D refinement, and

532   per-particle CTF refinement. Final 3D refinement and post-processing yielded maps

533   with global resolutions of 2.8 Å, according to the FSC = 0.143 criterion. Finally, the

534   local resolution was estimated using RELION-3. The processing strategy is illustrated in

535   Supplementary Fig. 4.

536   For the TA-1887-bound state dataset, 3,395,470 particles were initially selected from

537   4,383 micrographs, using the topaz-picking function in RELION-4. Particles were

538   extracted by downsampling to a pixel size of 3.32 Å/px. These particles were subjected

539   to several rounds of 2D and 3D classification. The best class contained 274,477

540   particles, which were then re-extracted with a pixel size of 1.30 Å/px and subjected to

541   3D refinement. Non-aligned 3D classification using a soft mask covering the proteins

542   and micelles resulted in three map classes. The best class from the 3D classification

23

543   contained 103,853 particles, which were subjected to 3D refinement, per-particle CTF

544   refinement, and 3D refinement. The resulting 3D model and particle set were resized to

545   1.11 Å/px and subjected to Bayesian polishing, 3D refinement, and per-particle CTF

546   refinement. Final 3D refinement and post-processing yielded maps with global

547   resolutions of 2.9 Å, according to the FSC = 0.143 criterion. Local resolution was

548   estimated using RELION-4. The processing strategy is illustrated in Supplementary Fig.

549   5.

550   For the sotagliflozin-bound state dataset, 5,242,427 particles were initially selected from

551   5,499 micrographs using the topaz-picking function in RELION-4. Particles were

552   extracted by downsampling to a pixel size of 3.32 Å/px. These particles were subjected

553   to several rounds of 2D and 3D classifications. The best class contained 823,369

554   particles, which were then re-extracted with a pixel size of 1.30 Å/px and subjected to

555   3D refinement. Non-aligned 3D classification using a soft mask covering the proteins

556   and micelles resulted in four classes of maps. The two good classes from the 3D

557   classification contained 227,811 particles, which were subjected to 3D refinement. The

558   resulting 3D model and particle set were resized to 1.11 Å/px and subjected to Bayesian

559   polishing, 3D refinement, and further non-aligned 3D classification using a soft mask

560   covering the proteins and micelles. The best class from the 3D classification contained

561   72,773 particles, which were subjected to 3D refinement, per-particle CTF refinement,

562   3D refinement, Bayesian polishing, 3D refinement, and per-particle CTF refinement.

563   The final 3D refinement and post-processing yielded maps with global resolutions of

564   3.1 Å, according to the FSC = 0.143 criterion. Finally, the local resolution was

565   estimated using RELION. The processing strategy is illustrated in Supplementary Fig.

566   6.

567   For the phlorizin-bound state dataset, 3,013,029 particles were initially selected from

568   3,159 micrographs using the Laplacian-of-Gaussian picking function in RELION-3.1[23]

569   and were used to generate two-dimensional (2D) models for reference-based particle

570   picking. Particles were extracted by downsampling to a pixel size of 3.32 Å/px. These

571   particles were subjected to several rounds of 2D and 3D classification. The best class

572   contained 324,355 particles, which were then re-extracted with a pixel size of 1.66 Å/px

573   and subjected to 3D refinement. The particles were subsequently subjected to micelle

574   subtraction and non-aligned 3D classification using a mask (excluding the micelles),

575   resulting in three map classes. The best class contained 76,485 particles, which were

576   then subjected to 3D refinement and reversion to the original particles. The particle set

577   was resized to 1.30 Å/px, and subjected to Bayesian polishing, 3D refinement, and

578   per-particle CTF refinement before the final 3D refinement and post-processing,

579   yielding a map with a global resolution of 3.3 Å according to the FSC = 0.143 criterion.

580   Finally, the local resolution was estimated using RELION-3. The processing strategy is

581   illustrated in Supplementary Fig. 8.

582

583   ***Model building and validation***

584   The models of the phlorizin-bound inward state of hSGLT2–MAP17 were manually

585   built, de novo, using the cryo-EM density map tool in COOT, facilitated by an

586   hSGLT2-homology model generated using Alphafold2[41]. After manual adjustment, the

587   models were subjected to structural refinement via the Servalcat pipeline in

588   REFMAC5[42] and manual real-space refinement in COOT. The models of the

589   dapagliflozin-, TA-1887-, sotagliflozin-, and canagliflozin-bound outward states were

590   built using the Alphafold2-derived hSGLT2-homology model as the starting model. The

591   3D reconstruction and model refinement statistics are summarized in Supplementary

592   Data Table 1. All molecular graphics figures were prepared using CueMol

593   (http://www.cuemol.org) and UCSF Chimera[43].

594

595

596   **Acknowledgements**

597   We thank Y. Lee and T. Nishizawa for technical advice on sample preparation; K.

598   Yamashita for technical advice on refinement using Servalcat; T. Saijo, T. Takahashi and

599   Y. Kamikozawa for technical advice on functional analyses; and M. Shiotani, C.

600   Kuriyama, and Y. Yamamoto for fruitful discussions about the inhibitory mechanism.

601   We thank the scientific staff of the cryo-EM facility of the University of Tokyo, and

602   especially Y. Kise, Y. Sakamaki, T. Kusakizako, H. Yanagisawa, A. Tsutsumi, M.

603   Kikkawa, and R. Danev.

604   This work was not supported by external funding.

605

606   **Author contributions**

607   M.H. designed the entire study. M.H. performed the cryo-EM analyses, with sample

608   preparation assistance from T.K.; M.H. and T.A. designed and performed the functional

609   analyses, with sample preparation assistance from M.H. and T.K. M.H. performed

610   model building and model refinement, with assistance from H.K. and K.M. M.H., T.A.,

611   N.T., I.M., and O.N. wrote and edited the manuscript, with help from all other authors.

612   M.H., T.A., I.M., and O.N. supervised the study.

613

Materials and correspondence

Masahiro Hiraizumi, Ikuko Miyaguchi, and Osamu Nureki

Competing interests:

Masahiro Hiraizumi, Tomoya Akashi, Kouta Murasaki, Hiroyuki Kishida, Taichi Kumanomidou, Nao Torimoto, and Ikuko Miyaguchi are employees of Mitsubishi Tanabe Pharma Corporation. Osamu Nureki is a co-founder of, and scientific advisor to, Curreio.

Data and materials availability

Cryo-EM density maps were deposited in the Electron Microscopy Data Bank under accession codes EMD-34673 (canagliflozin-bound state), EMD-34705 (dapagliflozin-bound state), EMD-34610 (TA-1887-bound state), EMD-34737 (sotagliflozin-bound state), and EMD-34823 (phlorizin-bound state). Atomic coordinates have been deposited in the Protein Data Bank under IDs 8HDH (canagliflozin-bound state), 8HEZ (dapagliflozin-bound state), 8HB0 (TA-1887-bound state), 8HG7 (sotagliflozin-bound state), and 8HIN (phlorizin-bound state). The datasets generated during and/or analysed during the current study are available from the corresponding author on reasonable request.

References

1. Maccari, R. & Ottanà, R. Sodium-Glucose Cotransporter Inhibitors as Antidiabetic Drugs: Current Development and Future Perspectives. *J. Med. Chem.* **65**, 10848–10881 (2022).

2. Wright, E. M., Loo, D. D. F. & Hirayama, B. A. Biology of Human Sodium

639   Glucose Transporters. *Physiol. Rev.* **91**, 733–794 (2011).

640   3.   Kanai, Y., Lee, W. S., Brown, D. & Hediger, M. A. The human kidney low
641   affinity Na+/glucose cotransporter SGLT2. Delineation of the major renal reabsorptive
642   mechanism for D-glucose. *J. Clin. Invest.* **93**, 397–404 (1994).

643   4.   Isaji, M. SGLT2 inhibitors: molecular design and potential differences in effect.
644   *Kidney Int.* **79**, S14–S19 (2011).

645   5.   Faillie, J.-L. Pharmacological aspects of the safety of gliflozins. *Pharmacol.*
646   *Res.* **118**, 71–81 (2017).

647   6.   Wright, E. M. SGLT2 Inhibitors: Physiology and Pharmacology. *Kidney360* **2**,
648   2027–2037 (2021).

649   7.   Lim, V. G. *et al.* SGLT2 Inhibitor, Canagliflozin, Attenuates Myocardial
650   Infarction in the Diabetic and Nondiabetic Heart. *JACC Basic Transl. Sci.* **4**, 15–26
651   (2019).

652   8.   Bhattacharya, S. *et al.* An exhaustive perspective on structural insights of
653   SGLT2 inhibitors: A novel class of antidiabetic agent. *Eur. J. Med. Chem.* **204**, 112523
654   (2020).

655   9.   Powell, D. R. *et al.* LX2761, a Sodium/Glucose Cotransporter 1 Inhibitor
656   Restricted to the Intestine, Improves Glycemic Control in Mice. *J. Pharmacol. Exp.*
657   *Ther.* **362**, 85–97 (2017).

658   10.   Powell, D. R. *et al.* LX4211 Increases Serum Glucagon-Like Peptide 1 and
659   Peptide YY Levels by Reducing Sodium/Glucose Cotransporter 1 (SGLT1)–Mediated
660   Absorption of Intestinal Glucose. *J. Pharmacol. Exp. Ther.* **345**, 250–259 (2013).

661   11.   Sands, A. T. *et al.* Sotagliflozin, a Dual SGLT1 and SGLT2 Inhibitor, as
662   Adjunct Therapy to Insulin in Type 1 Diabetes. *Diabetes Care* **38**, 1181–1188 (2015).

663   12.   del Alamo, D., Meiler, J. & Mchaourab, H. S. Principles of Alternating Access
664   in LeuT-fold Transporters: Commonalities and Divergences. *J. Mol. Biol.* **434**, 167746
665   (2022).

666   13.   Gyimesi, G., Pujol-Giménez, J., Kanai, Y. & Hediger, M. A. Sodium-coupled
667   glucose transport, the SLC5 family, and therapeutically relevant inhibitors: from
668   molecular discovery to clinical application. *Pflüg. Arch. - Eur. J. Physiol.* **472**,
669   1177–1206 (2020).

670   14.   Watanabe, A. *et al.* The mechanism of sodium and substrate release from the
671   binding pocket of vSGLT. *Nature* **468**, 988–991 (2010).

672   15.   Faham, S. *et al.* The Crystal Structure of a Sodium Galactose Transporter
673   Reveals Mechanistic Insights into Na$^+$/Sugar Symport. *Science* **321**, 810–814 (2008).

674   16.   Bisignano, P. *et al.* Inhibitor binding mode and allosteric regulation of

675   Na$^+$-glucose symporters. *Nat. Commun.* **9**, 5245 (2018).

676   17.   Han, L. *et al.* Structure and mechanism of the SGLT family of glucose
677   transporters. *Nature* **601**, 274–279 (2022).

678   18.   Coady, M. J. *et al.* MAP17 Is a Necessary Activator of Renal Na$^+$/Glucose
679   Cotransporter SGLT2. *J. Am. Soc. Nephrol.* **28**, 85–93 (2017).

680   19.   Niu, Y. *et al.* Structural basis of inhibition of the human SGLT2–MAP17
681   glucose transporter. *Nature* **601**, 280–284 (2022).

682   20.   Niu, Y. *et al.* Structural mechanism of SGLT1 inhibitors. *Nat. Commun.* **13**,
683   6440 (2022).

684   21.   Kawate, T. & Gouaux, E. Fluorescence-Detection Size-Exclusion
685   Chromatography for Precrystallization Screening of Integral Membrane Proteins.
686   *Structure* **14**, 673–681 (2006).

687   22.   Pédelacq, J.-D., Cabantous, S., Tran, T., Terwilliger, T. C. & Waldo, G. S.
688   Engineering and characterization of a superfolder green fluorescent protein. *Nat.*
689   *Biotechnol.* **24**, 79–88 (2006).

690   23.   Zivanov, J. *et al.* New tools for automated high-resolution cryo-EM structure
691   determination in RELION-3. *eLife* **7**, e42166 (2018).

692   24.   Kimanius, D., Dong, L., Sharov, G., Nakane, T. & Scheres, S. H. W. New tools
693   for automated cryo-EM single-particle analysis in RELION-4.0. *Biochem. J.* **478**,
694   4169–4185 (2021).

695   25.   Wahlgren, W. Y. *et al.* Substrate-bound outward-open structure of a
696   Na$^+$-coupled sialic acid symporter reveals a new Na$^+$ site. *Nat. Commun.* **9**, 1753
697   (2018).

698   26.   Sala-Rabanal, M. *et al.* Bridging the gap between structure and kinetics of
699   human SGLT1. *Am. J. Physiol.-Cell Physiol.* **302**, C1293–C1305 (2012).

700   27.   Coady, M. J., Wallendorff, B. & Lapointe, J.-Y. Characterization of the
701   transport activity of SGLT2/MAP17, the renal low-affinity Na$^+$-glucose cotransporter.
702   *Am. J. Physiol.-Ren. Physiol.* **313**, F467–F474 (2017).

703   28.   Hirayama, B. A. *et al.* Sodium-Dependent Reorganization of the Sugar-Binding
704   Site of SGLT1. *Biochemistry* **46**, 13391–13406 (2007).

705   29.   Kakinuma, H. *et al.* (1
706   *S*)-1,5-Anhydro-1-[5-(4-ethoxybenzyl)-2-methoxy-4-methylphenyl]-1-thio- D -glucitol
707   (TS-071) is a Potent, Selective Sodium-Dependent Glucose Cotransporter 2 (SGLT2)
708   Inhibitor for Type 2 Diabetes Treatment. *J. Med. Chem.* **53**, 3247–3261 (2010).

709   30.   Ohtake, Y. *et al.* Discovery of Tofogliflozin, a Novel *C*-Arylglucoside with an
710   *O* -Spiroketal Ring System, as a Highly Selective Sodium Glucose Cotransporter 2

(SGLT2) Inhibitor for the Treatment of Type 2 Diabetes. *J. Med. Chem.* **55**, 7828–7840 (2012).

31. Hummel, C. S. *et al.* Structural selectivity of human SGLT inhibitors. *Am. J. Physiol.-Cell Physiol.* **302**, C373–C382 (2012).

32. Nomura, S. *et al.* Novel Indole- *N* -glucoside, TA-1887 As a Sodium Glucose Cotransporter 2 Inhibitor for Treatment of Type 2 Diabetes. *ACS Med. Chem. Lett.* **5**, 51–55 (2014).

33. Ožegović, B., McNamara, P. D., Goldmann, D. R. & Segal, S. Binding of [3H] phlorizin to rat kidney plasma membranes. *FEBS Lett.* **43**, 6–8 (1974).

34. Ghezzi, C. *et al.* SGLT2 inhibitors act from the extracellular surface of the cell membrane. *Physiol. Rep.* **2**, e12058 (2014).

35. Hummel, C. S. *et al.* Glucose transport by human renal Na^+/D-glucose cotransporters SGLT1 and SGLT2. *Am. J. Physiol.-Cell Physiol.* **300**, C14–C21 (2011).

36. Quick, M., Loo, D. D. F. & Wright, E. M. Neutralization of a Conserved Amino Acid Residue in the Human Na^+/Glucose Transporter (hSGLT1) Generates a Glucose-gated H+ Channel. *J. Biol. Chem.* **276**, 1728–1734 (2001).

37. Nomura, S. *et al.* Discovery of Canagliflozin, a Novel *C* -Glucoside with Thiophene Ring, as Sodium-Dependent Glucose Cotransporter 2 Inhibitor for the Treatment of Type 2 Diabetes Mellitus. *J. Med. Chem.* **53**, 6355–6360 (2010).

38. Axel Kirchhofer *et al.* Modulation of protein properties in living cells using nanobodies. *Nat Struct Mol Biol* **17**, 133–138 (2010).

39. Mastronarde, D. N. Automated electron microscope tomography using robust prediction of specimen movements. *J. Struct. Biol.* **152**, 36–51 (2005).

40. Rohou, A. & Grigorieff, N. CTFFIND4: Fast and accurate defocus estimation from electron micrographs. 18 (2019).

41. Jumper, J. *et al.* Highly accurate protein structure prediction with AlphaFold. *Nature* **596**, 583–589 (2021).

42. Yamashita, K., Palmer, C. M., Burnley, T. & Murshudov, G. N. Cryo-EM single-particle structure refinement and map calculation using *Servalcat*. *Acta Crystallogr. Sect. Struct. Biol.* **77**, 1282–1291 (2021).

43. Pettersen, E. F. *et al.* UCSF Chimera--A visualization system for exploratory research and analysis. *J. Comput. Chem.* **25**, 1605–1612 (2004).

Figure legends

Figure 1. Biochemical and cryo-EM studies of the human SGLT2–MAP17 heterodimer.

a Topological diagram of the hSGLT2–MAP17 heterodimer. Inverted repeats (IRs) are represented as light blue and light brown. The Y-shape indicates an N-glycosylation site. Disulfide bonds are shown as orange sticks. A signal peptide (SP) and super-folder (sf) GFP were fused to the N-terminus of hSGLT2. The dotted line indicates the site of protease activity. **b** Chemical structures of the substrates and a representative gliflozin. **c,** FSEC profiles of various types of GFP-tagged hSGLT2 without MAP17. Arrows indicate elution positions of the hSGLT2–MAP17 heterodimer and free GFP (GFP). **d** α-MG uptake in hSGLT2 and MAP17 expressing cells in the absence (white) or presence (orange) of 500 nM canagliflozin. Each column represents mean ± SEM (n = 4, biological replicates). **e** Canagliflozin (30 nM) binding assay for the hSGLT2- and MAP17-expressing cell membrane fraction. Each column represents mean ± SEM (n = 3, technical replicates). **f,** Overall structure of the human SGLT2-MAP17 complex. Cryo-EM maps (top) and ribbon models (bottom). The same color scheme was used throughout the manuscript, except for Fig. 4.

Figure 2. SGLT2-inhibitor-binding site of the outward-facing conformation.

a, Cross-sections of the electrostatic surface potentials at the SGLT2 inhibitor-binding site. The potentials were displayed as a color gradient from red (negative) to blue (positive). **b,** Interactions between canagliflozin and hSGLT2. Canagliflozin and its interacting residues are shown as sticks. The hydrogen bonds are indicated by the black dashed lines. **c,** Conformation change from outward-opening (color) to inward-opening (grey) around the Na2 binding site. View from the lateral side of the

768   plasma membrane (left) and from the cytoplasmic side (right). **d**,

769   Concentration-dependent binding evaluation of canagliflozin in the presence and

770   absence of Na$^+$. Each point represents the mean ± SEM (n = 3, technical replicates).

771   **e–h**, Chemical structures of inhibitors and their interactions with hSGLT2:

772   sotagliflozin (**e**), TA-1887 (**f**), and dapagliflozin (**g**) in this study, and of empagliflozin

773   (**h**) (previously reported; [19]).

774

775   Figure 3. Phlorizin binding site of the inward-open conformation.

776   **a**, The inward-open conformation of the hSGLT2–MAP17 complex. Cryo-EM maps

777   (left) and ribbon models (right). **b,** Chemical structures of phlorizin and phloretin. **c**,

778   Interactions between phlorizin and hSGLT2. **d**, Concentration-dependent binding of

779   phlorizin to the wild-type hSGLT2. Each point represents the mean ± SEM (n = 3,

780   technical replicates). **e**, Concentration-dependent binding of phlorizin in wild-type and

781   mutant hSGLT2. Each point represents the mean ± SEM (n = 3, technical replicates). **f,**

782   Eadie-Hofstee plot analysis of phlorizin binding in wild-type and mutant hSGLT2. Each

783   point represents the mean ± SEM (n = 3, technical replicates). **g**,

784   Concentration-dependent binding of phloretin in wild-type and mutant hSGLT2. Each

785   point represents the mean ± SEM (n = 3, technical replicates). **h**, Uptake assay of α-MG

786   in wild-type and mutant hSGLT2. Each column represents mean ± SEM (n = 4,

787   biological replicates). **i**, Inhibitory effect of phlorizin on α-MG uptake by wild-type and

788   mutant hSGLT2. Each point represents the mean ± SEM (n = 4, biological replicates).

789

790   Figure 4. Comparison of the outward-facing and inward-open conformations of

791   hSGLT2.

792   **a**, The outward-facing (colored) and inward-open (transparent) structures when their

793   bundle domains (TM1, -2, -6, and -7; red) are superimposed. MAP17 (grey) and TM13

794   (light orange) overlap well between the conformations, but the hash domain (TM3, -4,

795   -8, -9; blue), gate helices (TM5, -10; green), TM0, -11 and -12 (light orange) are in the

796   inward-opening conformation. **b**, The outward-facing conformation of the

797   hSGLT2–MAP17 complex with canagliflozin viewed from the exoplasm (left), side

798   (center), and cytoplasm (right). **c**, Substrate sugar-binding site and external vestibule of

799   the outward-facing conformation from the exoplasm. **d**, The inward-open conformation

800   of the hSGLT2–MAP17 complex with phlorizin viewed from the exoplasm (left), side

801   (center), and cytoplasm (right). **e**, Substrate sugar-binding site and external vestibule of

802   the inward-open conformation from the exoplasm.

803

804   Figure 5. Proposed SGLT2 transport and inhibition mechanism.

805   The bundle domain is anchored to the membrane with MAP17, and the rest of the

806   transporter undergoes a conformational change according to an alternating-access

807   mechanism. Upon sodium binding, the transporter opens outward to allow a substrate or

808   inhibitors to bind. Upon substrate binding, the inner gate opens and sodium and glucose

809   are released into the cell. After sodium and glucose are released, the transporter forms

810   an inward-open structure and phlorizin and phloretin bind to this structure, inhibiting

811   glucose transport.

812

813

814   Supplementary Figure 1. Biochemical characterization of the hSGLT2–MAP17

815   complex.

816   (a) Representative size-exclusion chromatography profile of hSGLT2–MAP17. (b)

817   SDS-PAGE analysis of the hSGLT2–MAP17 peak fractions via size-exclusion

818   chromatography (SEC) purification. (c) SGLT2 inhibitors (25 nM) binding to the crude

819   membrane expressing hSGLT2 and MAP17. (d) FSEC profiles for various mutations of

820   sfGFP-tagged hSGLT2 with MAP17. The arrows indicate the elution positions of the

821   hSGLT2–MAP17 heterodimer and the free GFP (GFP). (e) Canagliflozin binding to the

822   crude membrane expressing wild-type hSGLT2 and mutants. Crude membranes were

823   incubated with 30 nM canagliflozin and binding was measured by LC-MS/MS. Data are

824   shown as mean ± SEM (n = 3). (f) Time-course of hSGLT2-mediated α-MG uptake.

825   α-MG uptake (500 μM) by hSGLT2-expressing cells and mock cells was examined.

826   Each point represents mean ± SEM (n = 3). (g) Chromatograms of α-MG in the lysates

827   of untreated mock cells (No treatment), mock cells incubated with α-MG (Mock), and

828   hSGLT2- and MAP17-expressing cells incubated with α-MG (hSGLT2).

829

830   Supplementary Figure 2. Sequence alignment of SGLT.

831   Sequence alignment of hSGLT2 (UniProt: P31639), mSGLT2 (UniProt: Q92317),

832   hSGLT1 (UniProt: P13866), *Vibrio parahaemolyticus* SGLT (UniProt: P96169), and

833   *Proteus mirabilis* HI4320 sialic acid symporter (UniProt: B4EZY7), performed using

834   Clustal Omega. Conserved transmembrane helices of hSGLT2 are indicated above the

835   sequences. The similarly conserved residues are indicated by red letters. The residues at

836   the conserved Na2 and Na3 sites of SGLT are highlighted with pink circles above or

837   white circles below the alignment, respectively.

838

839   Supplementary Figure 3. Data processing of the canagliflozin-bound state.

840   (a) Representative cryo-EM image of the hSGLT2–MAP17 complex in the presence of

841   canagliflozin. (b) Data processing workflow of single-particle image-processing and

842   local-resolution analysis. Particles were separated into three groups via non-aligned 3D

843   classification, with the mask (without micelles) shown in yellow. (c) Cross-validation

844   FSC curves for map-to-model fitting. (d) Angular distributions of the final

845   reconstruction.

846

847   Supplementary Figure 4. Data processing of the dapagliflozin-bound state.

848   (a) Representative cryo-EM image of the hSGLT2–MAP17 complex in the presence of

849   dapagliflozin. (b) Data processing workflow of single-particle image-processing and

850   local-resolution analysis. Particles were separated into four groups by non-aligned 3D

851   classification, with the mask (without micelles) shown in transparent white. (c)

852   Cross-validation FSC curves for map-to-model fitting. (d) Angular distributions of the

853   final reconstruction.

854

855   Supplementary Figure 5. Data processing of the TA-1887-bound state.

856   (a) Representative cryo-EM image of the hSGLT2–MAP17 complex in the presence of

857   TA-1887. (b) Data processing workflow of single-particle image-processing and

858   local-resolution analysis. Particles were separated into three groups via non-align 3D

859 classification, with the mask covering the proteins and micelle shown in transparent

860 white. (c) Cross-validation FSC curves for map-to-model fitting. (d) Angular

861 distributions of the final reconstruction.

862

863 Supplementary Figure 6. Data processing of the sotagliflozin-bound state.

864 (a) Representative cryo-EM image of the hSGLT2–MAP17 complex in the presence of

865 sotagliflozin. (b) Data processing workflow of single-particle image-processing and

866 local-resolution analysis. Particles were separated into three groups via two rounds of

867 non-aligned 3D classification, with the mask covering the proteins and micelles shown

868 in transparent white. (c) Cross-validation FSC curves for map-to-model fitting. (d)

869 Angular distributions of the final reconstruction.

870

871 Supplementary Figure 7. The outward-opening model of hSGLT2–MAP17 in the

872 density maps.

873 The cryo-EM density and atomic model of each segment of the outward-opening model

874 hSGLT2–MAP17, inhibitors, and glycosylation sites, contoured to 3.0 σ, 4.0 σ, and 2.0

875 σ, respectively. Red spheres: water molecules around the inhibitors.

876

877 Supplementary Figure 8. Data processing of the phlorizin-bound state.

878 (a) Representative cryo-EM image of the hSGLT2–MAP17 complex in the presence of

879 phlorizin. (b) Data processing workflow of single-particle image-processing and

880 local-resolution analysis. Particles were separated into three groups by non-aligned 3D

881 classification, with the mask covering the proteins (without micelles) shown in yellow.

882 (c) Cross-validation FSC curves for map-to-model fitting. (d) Angular distributions of

883   the final reconstruction.

884

885   Supplementary Figure 9. Inward-open model of hSGLT2–MAP17 in the density maps.

886   The cryo-EM density and atomic models of each segment of the inward-open model of

887   hSGLT2–MAP17, phlorizin, and glycosylation sites, contoured to 2.9 σ, 2.7 σ, and 2.7 σ,

888   respectively.

889

890   Supplementary Figure 10. MAP17 and SGLT2 interaction site.

891   The density of the lipid molecule (orange) is observed between MAP17 and SGLT2.

892

893   Supplementary Figure 11. Sodium ion-binding sites of SGLT2

894   (a) The sodium ion-binding Na2 sites of dapagliflozin, canagliflozin, TA-1887, and

895   sotagliflozin are shown. (b) Sites in SGLT2 corresponding to Na3 sites where the other

896   sodium ion binds in SGLT1. No electron density corresponding to a sodium ion can be

897   observed. (c, d) The sodium ion-binding Na2 sites, and the sites corresponding to Na3

898   sites of the phlorizin-bound inward-open conformation. The phlorizin binding site is

899   near the Na2 and Na3 sites.

900

901   Supplementary Figure 12. Comparison of the inward conformation of other SGLT

902   structures.

903   Structural comparison of sites corresponding to the intracellular phlorizin-binding sites

904   of SGLT2. From left to right, inward-occluded conformation of hSGLT1,

905   inward-occluded conformation of vSGLT, and inward-open conformation of vSGLT.

906   The structures

37

907   are viewed from the membrane side.

908

909   Supplementary Data Table 1.

910   Data collection, processing, model refinement, and validation. Clash scores, rotamer

911   outliers, and Ramachandran plots were calculated using the Servalcat pipeline.

912

913   Supplementary Data Table 2.

914   Kinetic parameters of canagliflozin binding in the membrane fraction of

915   hSGLT2-expressing and MAP17-expressing cells, in the presence or absence of Na^+.

916

917   Supplementary Data Table 3.

918   Kinetic parameters of phlorizin and phloretin binding in the membrane fraction of

919   wild-type cells or cells expressing mutated hSGLT2 and MAP17.

920

921   Supplementary Data Table 4.

922   IC50 values of phlorizin in α-MG uptake by wild-type and mutant hSGLT2.

923

924   Supplementary Movie 1.

925   Movement of SGLT2 during sugar uptake, as predicted from the cryo-EM structures.

926   The bundle domain (TM1, -2, -6, -7; red) functions as the axis together with MAP17
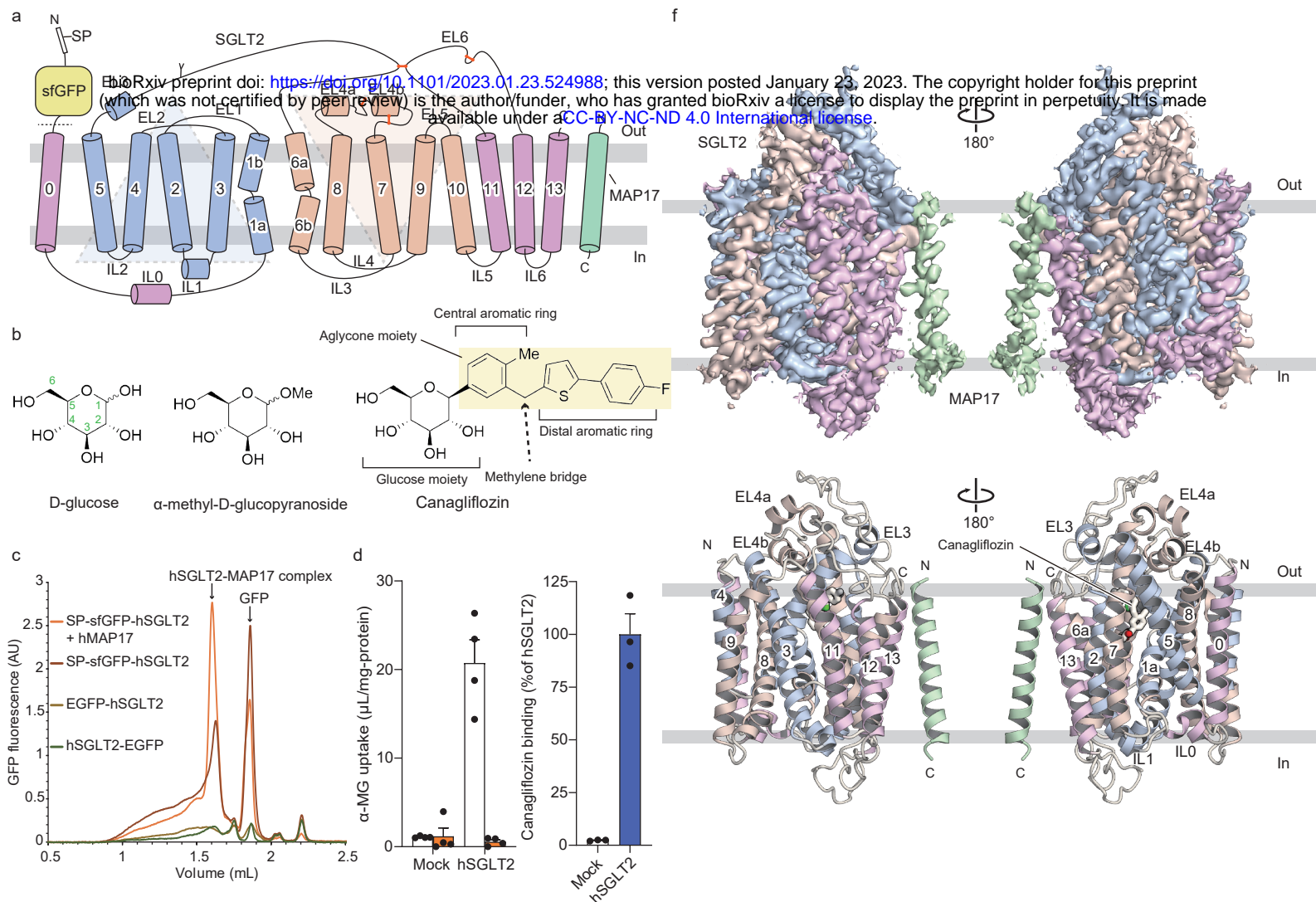
927   (gray). TM13 (light orange), the hash domains (TM3, -4, -8, -9; blue), and the gate

928   helices TM5 and TM10 (green) and TM0, TM11, and -12 (light orange) move

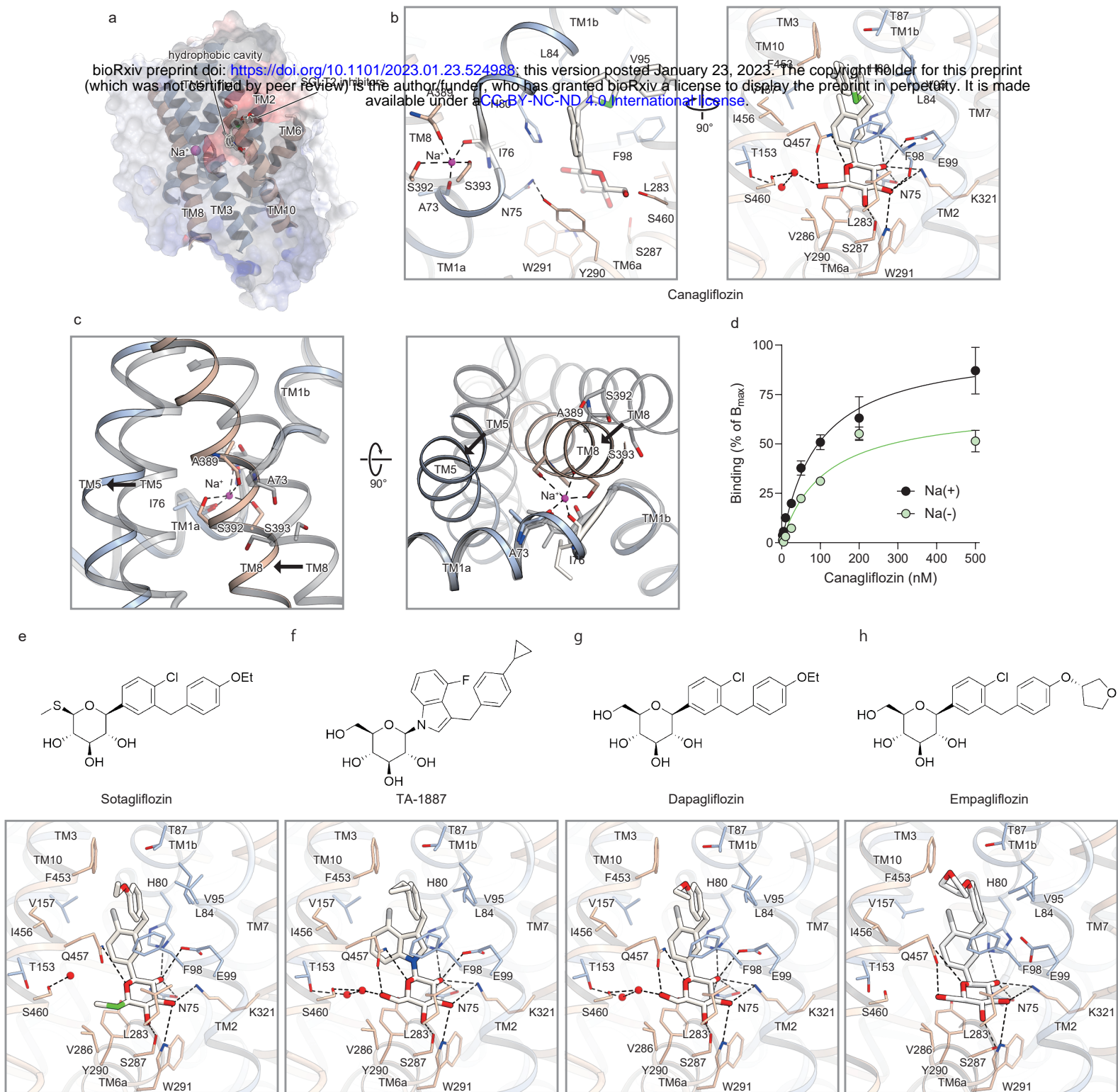929   significantly, transporting the sugar to the intracellular side.

930

931

**Figure 1. Biochemical and cryo-EM studies of the human SGLT2–MAP17 heterodimer.**

a Topological diagram of the hSGLT2–MAP17 heterodimer. Inverted repeats (IRs) are represented as light blue and light brown. The Y-shape indicates an N-glycosylation site. Disulfide bonds are shown as orange sticks. A signal peptide (SP) and super-folder (sf) GFP were fused to the N-terminus of hSGLT2. The dotted line indicates the site of protease activity. b Chemical structures of the substrates and a representative gliflozin. c, FSEC profiles of various types of GFP-tagged hSGLT2 without MAP17. Arrows indicate elution positions of the hSGLT2–MAP17 heterodimer and free GFP (GFP). d α-MG uptake in hSGLT2 and MAP17 expressing cells in the absence (white) or presence (orange) of 500 nM canagliflozin. Each column represents mean ± SEM (n = 4, biological replicates). e Canagliflozin (30 nM) binding assay for the hSGLT2- and MAP17-expressing cell membrane fraction. Each column represents mean ± SEM (n = 3, technical replicates). f, Overall structure of the human SGLT2-MAP17 complex. Cryo-EM maps (top) and ribbon models (bottom). The same color scheme was used throughout the manuscript, except for Fig. 4.

Figure 2. SGLT2-inhibitor-binding site of the outward-facing conformation.

a, Cross-sections of the electrostatic surface potentials at the SGLT2 inhibitor-binding site. The potentials were displayed as a color gradient from red (negative) to blue (positive). b, Interactions between canagliflozin and hSGLT2. Canagliflozin and its interacting residues are shown as sticks. The hydrogen bonds are indicated by the black dashed lines. c, Conformation change from outward-opening (color) to inward-opening (grey) around the Na2 binding site. View from the lateral side of the plasma membrane (left) and from the cytoplasmic side (right). d, Concentration-dependent binding evaluation of canagliflozin in the presence and absence of Na+. Each point represents the mean ± SEM (n = 3, technical replicates). e–h, Chemical structures of inhibitors and their interactions with hSGLT2: sotagliflozin (e), TA-1887 (f), and dapagliflozin (g) in this study, and of empagliflozin (h) (previously reported; [19]).
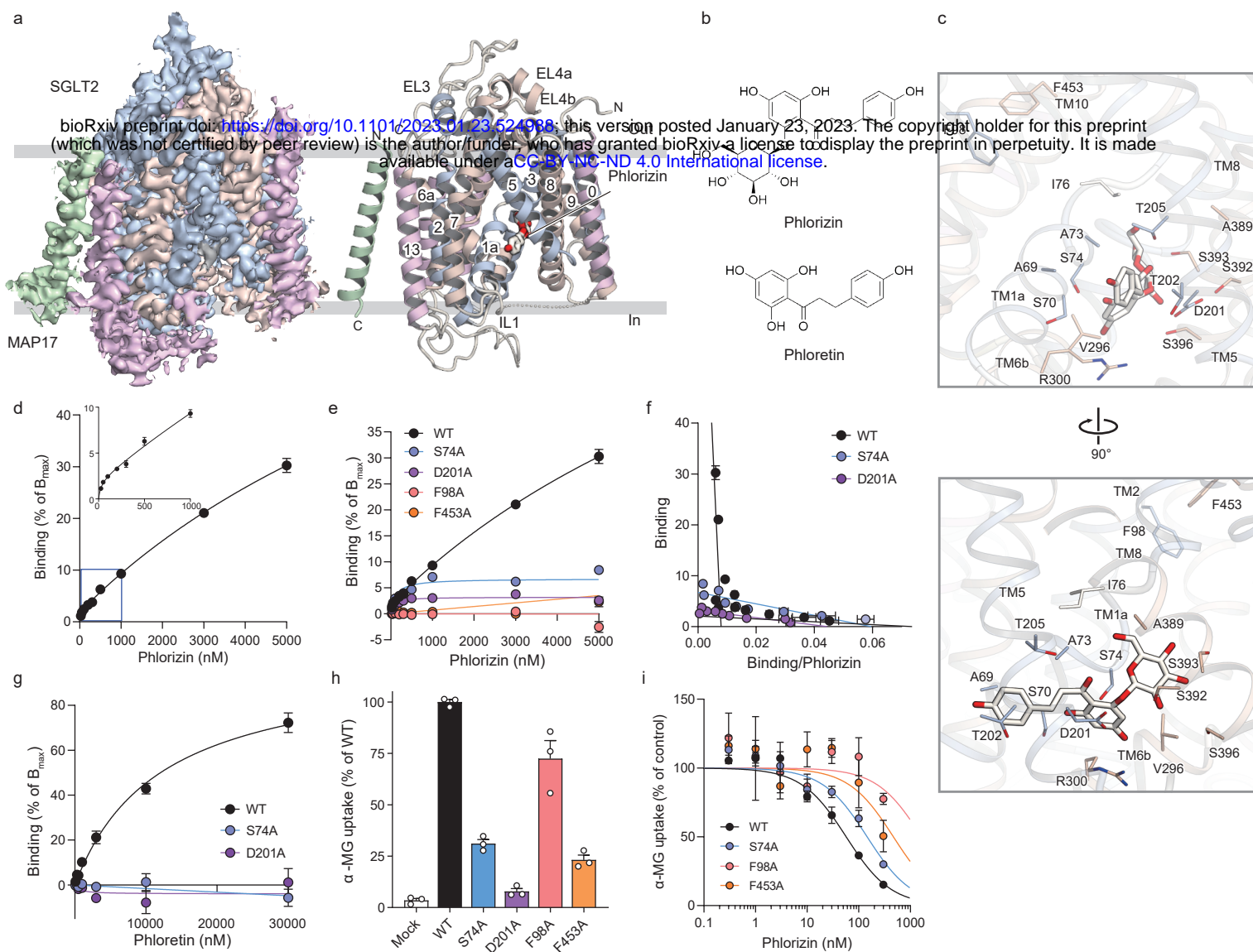
Figure 3. Phlorizin binding site of the inward-open conformation.

a, The inward-open conformation of the hSGLT2–MAP17 complex. Cryo-EM maps (left) and ribbon models (right). b, Chemical structures of phlorizin and phloretin. c, Interactions between phlorizin and hSGLT2. d, Concentration-dependent binding of phlorizin to the wild-type hSGLT2. Each point represents the mean ± SEM (n = 3, technical replicates). e, Concentration-dependent binding of phlorizin in wild-type and mutant hSGLT2. Each point represents the mean ± SEM (n = 3, technical replicates). f, Eadie-Hofstee plot analysis of phlorizin binding in wild-type and mutant hSGLT2. Each point represents the mean ± SEM (n = 3, technical replicates). g, Concentration-dependent binding of phloretin in wild-type and mutant hSGLT2. Each point represents the mean ± SEM (n = 3, technical replicates). h, Uptake assay of α-MG in wild-type and mutant hSGLT2. Each column represents mean ± SEM (n = 4, biological replicates). i, Inhibitory effect of phlorizin on α-MG uptake by wild-type and mutant hSGLT2. Each point represents the mean ± SEM (n = 4, biological replicates).
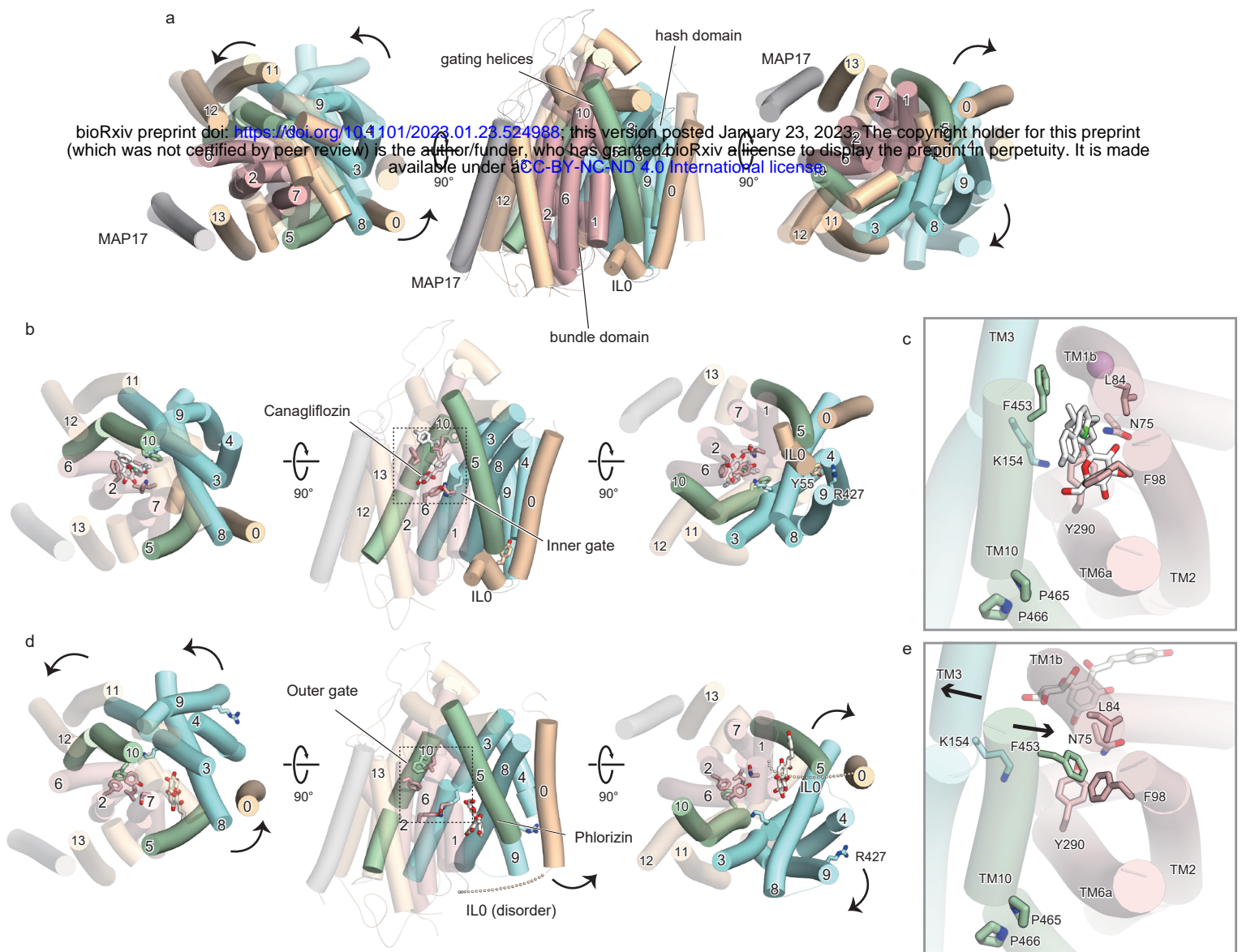
Figure 4. Comparison of the outward-facing and inward-open conformations of hSGLT2.

a, The outward-facing (colored) and inward-open (transparent) structures when their bundle domains (TM1, -2, -6, and -7; red) are superimposed. MAP17 (grey) and TM13 (light orange) overlap well between the conformations, but the hash domain (TM3, -4, -8, -9; blue), gate helices (TM5, -10; green), TM0, -11 and -12 (light orange) are in the inward-opening conformation. b, The outward-facing conformation of the hSGLT2–MAP17 complex with canagliflozin viewed from the exoplasm (left), side (center), and cytoplasm (right). c, Substrate sugar-binding site and external vestibule of the outward-facing conformation from the exoplasm. d, The inward-open conformation of the hSGLT2–MAP17 complex with phlorizin viewed from the exoplasm (left), side (center), and cytoplasm (right). e, Substrate sugar-binding site and external vestibule of the inward-open conformation from the exoplasm.
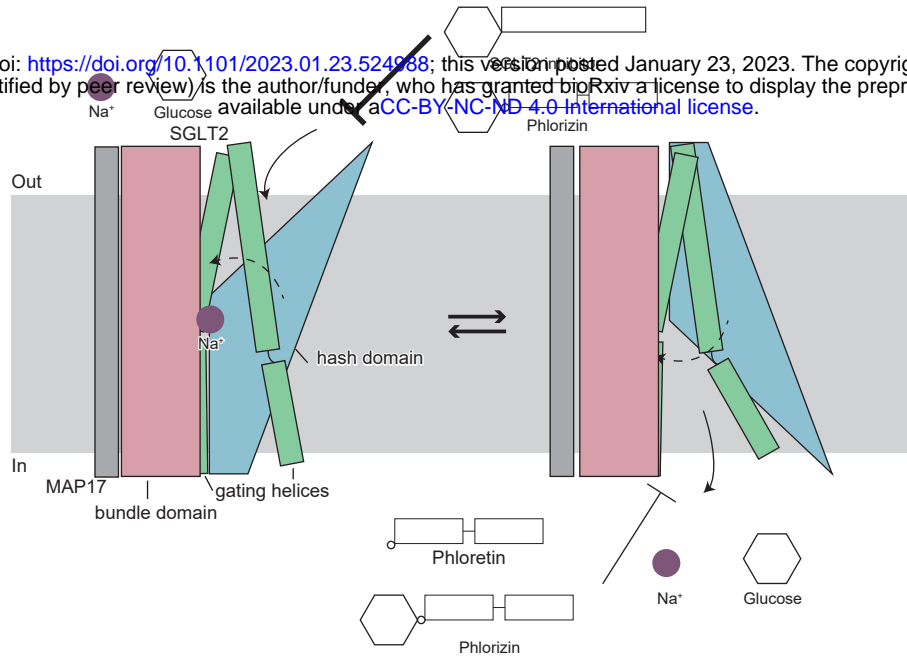
Figure 5. Proposed SGLT2 transport and inhibition mechanism.

The bundle domain is anchored to the membrane with MAP17, and the rest of the transporter undergoes a conformational change according to an alternating-access mechanism. Upon sodium binding, the transporter opens outward to allow a substrate or inhibitors to bind. Upon substrate binding, the inner gate opens and sodium and glucose are released into the cell. After sodium and glucose are released, the transporter forms an inward-open structure and phlorizin and phloretin bind to this structure, inhibiting glucose transport.